

Rough-Surface Shadowing of Self-Affine Random Rough Surfaces

Hannu Parviainen, Karri Muinonen

Observatory, B.O. Box 14, FI-00014 University of Helsinki, Finland

Abstract

Light scattering from self-affine homogeneous isotropic random rough surfaces is studied using the ray-optics approximation. Numerical methods are developed to accelerate the first-order scattering simulations from surfaces represented as single-connected single-valued random fields, and to store the results of the simulations into a numerical reflectance model. Horizon mapping and marching methods are developed to accelerate the simulation. Emphasis is given to the geometric shadowing and masking effects as a function of surface roughness, especially, to the azimuthal rough-surface shadowing effect.

Key words: light scattering; random rough surfaces; ray tracing; fractional Brownian motion; azimuthal shadowing effect; rough-surface shadowing

1. Introduction

Scattering of light from rough surfaces has been a topic of extensive study for several decades. Both theoretical and experimental research is carried out in many areas of physics. The amount of empirical research is vast, including both observational data—from Earth-based to space-probe observations—as well as strictly controlled laboratory measurements, and the increase of computational power in last decades has allowed application of advanced numerical methods.

Despite the advancement of the analytic rough-surface light scattering models, they are limited by necessity to simplified surface-roughness structures. Exact solutions to the rough-surface scattering have been derived for simple periodic structures, but realistic surfaces occurring in nature cannot be well represented with such. Natural surfaces show roughness at all scales—from the large-scale variations describing the general shape of the object down to the molecular, and ultimately atomic, structure of the medium. These roughness variations over different size scales can often be considered to be of self-affine fractal nature: the resolved roughness is a function of the scale of the observation. More realistic scattering models have been devised for several statistical random rough surface models, but fractal surfaces are still beyond analytic approach. Currently numerical simulation is the most valid method to test the applicability of the analytic scattering models, and the only method when it comes to the understanding of scattering by complex self-affine rough surfaces.

The theory of light scattering from planetary regoliths has been studied in depth by Lumme, Bowell and Irvine [1,2], who introduced a scattering model for a rough cratered surface and tested its validity

Email addresses: hannu@astro.helsinki.fi (Hannu Parviainen), muinonen@cc.helsinki.fi (Karri Muinonen).

against observational data. Hapke introduced his own analytic reflectance model derived from the equation of radiative transfer [3], with a correction for macroscopic surface roughness [4]. Later Lumme, Peltoniemi and Irvine [5] introduced a model for diffuse reflection from stochastically bounded semi-infinite medium based on Gaussian statistics, which was used to derive an average single-particle phase function for the lunar regolith [6]. Numerical studies have been carried out by Peltoniemi [7], who studied light scattering from closely-packed particulate medium. Shkuratov et al. have used numerical simulations together with photometric and polarimetric laboratory measurements of samples simulating the structure of planetary regoliths [8,9]. Shepard and Campbell [10,11,12] have studied geometric shadowing from fractal surfaces. Their study was focused on the behavior of the shadowing function when the surface is viewed from nadir, and showed that many of the currently used analytical shadowing functions can be well fitted to results obtained from self-affine fractional Brownian motion (fBm) surfaces. The roughness of natural surfaces has been shown to often follow fractal self-affine statistic, spanning all the observable scales. Thus, the fBm-model has been shown to allow for more realistic modeling of natural rough surfaces than the more frequently used models with a single major scale for roughness features.

The rough-surface shadowing and masking effects on light scattering are studied in this paper as a function of the angle of incidence θ_i and surface roughness model specific parameters (P_1, P_2) (described later in more detail) within the limits of the first-order geometric-optics approximation. All of the interactions of a single ray are considered to take place inside a single surface element, and the size of the surface curvature is considered to be substantially larger than the wavelength of the radiation. Special emphasis is given to the azimuthal shadowing and masking effect, caused by the self-shadowing of the surface. A comparison is made between two different surface roughness models: Gaussian correlation and generalized fractional Brownian motion (fBm). The Gaussian correlation model is good for its simplicity, but is not well fit to mimic natural rough surfaces, for which the self-affine fractal fBm-surfaces are more suited. The simulation is calculated over the full hemisphere (θ_e, ϕ_e) discretized using recursive spherical quadtree model for each set of free simulation parameters (θ_i, P_1, P_2) . The results over the hemisphere are saved into a numerical scattering model which allows interpolation inside the five-dimensional parameter space $(P_1, P_2, \theta_i, \theta_e, \phi_e)$ mixing spherical and Cartesian bases. The model can be used in varying inversion problems, such as statistical photoclinometry [13] and asteroid studies, to estimate the surface roughness properties.

2. Theory

2.1. Geometric Rough-Surface Shadowing and Masking Effects

In the regime of geometric optics, surface roughness has a notable effect on the radiation scattered from the surface. The surface features can shadow the surface from incident radiation, and mask the reflection from the irradiated parts. For a homogeneous isotropic surface with certain roughness statistics, the geometric self-shadowing and self-masking can be combined into a shadowing/masking function $S(\theta_i, \phi_i, \theta_e, \phi_e)$, which in the single-scattering approximation is independent of the underlying reflectance model. The shadowing/masking function gives the probability for a point visible to the observer to be illuminated as a function of the incidence angles (θ_i, ϕ_i) and the emergence angles (θ_e, ϕ_e) [14].

Exact formulation of the combined shadowing and masking function is currently possible only for a few simplified surface roughness models, and a numerical simulation is necessary when more realistic surfaces are of interest. Roughness models with self-affine properties, especially suited for mimicking many complex natural surfaces, are of special interest.

While a spectrum of advanced reflectance models have been developed with geometric shadowing as a function of θ_i and θ_e calculated by analytical means for several types of surface roughness, the ϕ_e dependence has generally been left out from the calculations because of the major increase in mathematical complexity. Neither do these reflectance models take the fractal nature of the surface roughness into account. While analytically difficult to model, surfaces with fractal properties can be simulated numerically, and the ϕ_e dependence can be included in the simulations. Numerical simulations allow the study of the azimuthal shadowing effect as a function of surface roughness, and the generation of a numerical rough-surface scatter-

ing model which can be evaluated as a function of viewing geometry, and the surface-roughness statistics.

2.2. Numerical Rough-Surface Reflectance Model

When the light scattering properties of a single surface element are considered to follow from a theoretical scattering model, a numerical rough-surface-corrected version of the model can be obtained from the simulations. Now, in addition to the shadowing and masking effects, the distribution of normals of the irradiated surface elements visible to a certain direction will alter the total observed reflectance of the surface.

Bidirectional reflectance-distribution function (BRDF) [15,16,17] f_r is defined as the ratio between the reflected radiance L_r and total irradiance E of the surface element as

$$f_r(\theta_i, \phi_i, \theta_r, \phi_r) = \frac{L_r(\theta_i, \phi_i, \theta_r, \phi_r)}{E}. \quad (1)$$

Considering unidirectional incident radiation ($E = \mu_0 F$) and isotropic surfaces, for which we can use symmetry relations to remove the explicit ϕ_i and ϕ_r dependence with their difference $\Delta\phi$, BRDF can be expressed as

$$f_r(\mu_0, \mu, \Delta\phi) = \frac{L_r(\mu_0, \mu, \Delta\phi)}{\mu_0 F}, \quad (2)$$

where $\mu_0 = \cos \theta_i$ and $\mu = \cos \theta_r$. Two basic reflectance functions are considered in current paper: the perfect diffuse Lambertian reflectance function $f_{r,L}$, and a more realistic Lommel-Seeliger reflectance function $f_{r,LS}$. These are respectively

$$f_{r,L} = \frac{\lambda_0}{\pi} \mu_0 F, \quad (3)$$

$$f_{r,LS} = P(\alpha) \frac{\tilde{\omega}}{4\pi} \frac{\mu_0}{\mu + \mu_0} F, \quad (4)$$

where $P(\alpha)$ is the phase function, $\tilde{\omega}$ the single scattering albedo, and λ_0 the Lambertian albedo. Since λ_0 and $\tilde{\omega}$ are nothing but multiplicative factors, when considering the first-order scattering, they are set to unity in the study. The phase function $P(\alpha)$ is also set to constant $P(\alpha) = 1$ to constrain the number of free parameters of the scattering model.

The major problem with a numerical reflectance model is how one can store and interpolate a five-dimensional function ($[H, l, \sigma, \theta_i, \theta_r, \Delta\phi]$), where H , l and σ are surface roughness parameters, of both Cartesian and spherical spaces with sufficient angular resolution. Several methods have been implemented to overcome this problem in previous studies, including spherical and hemispherical harmonics [18,19,20,21], Zernike polynomials [22], and spherical wavelets [23]. Hemispherical harmonics [21] was chosen for their computational efficiency and close relation to the well-known spherical harmonics.

2.3. Surfaces

Surfaces are represented as two-dimensional isotropic homogeneous random fields [24,25,26] specified by the autocorrelation function $C(r)$ [27] or, equivalently, spectral density function $S(f)$ [28]. The distribution of heights follows Gaussian statistics, and is defined by the standard deviation σ . The field realizations are periodic in x and y , with length of the period L .

Generation of a surface realization is based on the spectral synthesis method [27,17,29]. The surface statistics determine the power spectrum of the surface features in the frequency domain, and a surface realization is generated by transforming a randomized realization of the power spectrum to the spatial domain using fast Fourier transform (FFT).

Two different roughness types were chosen for the study: Gaussian correlation and general fractional Brownian motion models. Surfaces with Gaussian correlation between drops show roughness features of a certain scale, determined by the correlation length l , while the fBm-surfaces are of self-affine fractal nature showing roughness features of all scales, determined by the Hurst exponent H . The difference between the two models is illustrated in Fig. 1, where the fBm surface and Gaussian surface realization have identical $\frac{\sigma}{L}$.

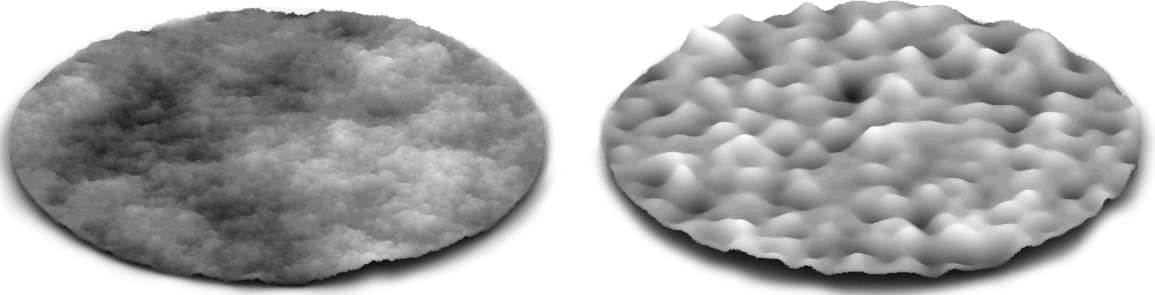


Figure 1. An fBm-surface realization with $H = 0.5$ and a surface realization with Gaussian correlation with $\frac{l}{L} = 0.025$. The standard deviation of heights $\frac{\sigma}{L} = 0.01$ is equal for both surfaces.

The radially symmetric spectral density functions for the Gaussian and fBm roughness models are

$$S_{Gauss}(\mathbf{k}) = \frac{l}{2\sqrt{\pi}} \exp\left(-\frac{|\mathbf{k}|^2 l^2}{4}\right), \quad (5)$$

$$S_{fBm}(\mathbf{k}) = |\mathbf{k}|^{-(H+1)}, \quad (6)$$

where $|\mathbf{k}|$ is the wavenumber. The correlation length is the distance where the correlation between drops down to e^{-1} and the Hurst exponent is related to the fractal dimension D of the surface as $H = 3 - D$.

3. Numerical Methods

3.1. Overview

The simulation is carried out in the ray-optics regime. The surface curvature radii in the simulation are considered to be much larger than the wavelength of light (tangent-plane approximation), and all the interactions of a single ray of light can be considered to take place inside a single surface element (first-order scattering approximation). For numerical calculations, both the surface and the integrating hemisphere are tessellated into discrete polygonal elements. The scattering model space is discretized for the θ_i angle of the incident radiation, and for the two surface roughness parameters ($[H, l], \sigma$).

The simulation consists of selecting n_p sample points p_j from a surface realization s_i , computing the highest unshadowed value θ_i for p_j , computing the solid area elements of the integrating hemisphere visible from p_j , and adding the contribution $F_{pj}(\theta_i, \phi_i, \theta_e, \phi_e)$ to each of the visible solid area element for each discrete value of θ_i . The simulation is repeated for n_s surface realizations, and the outcome is the ensemble average of the radiance from surface points visible to a direction of each of the solid area elements as a function of θ_i . If there is no BRDF assigned to the elements of the surface, the output is the geometric shadowing and masking function. Finally, the output is expanded into hemispherical harmonic coefficients for each θ_i , and the coefficients are saved to represent the model for the chosen set of parameters H and σ .

While the entire simulation could be done using basic ray-tracing techniques, the use of specialized optimization methods can increase the computation speed dramatically. The decreased computation time allows for more accurate simulations, and a reliable study of different effects as a function of the surface roughness parameters. The surface sample points p_j are selected from the surface plane using stratified Monte Carlo sampling [30], which offers a good trade-off between speed and the quality of sampling. A horizon map generated for the surface is used to find the highest unshadowed value for the angle of the incident radiation (θ_i) for each sample point p_j . The integrating hemisphere is represented as a recursive hierarchical geometry with discrete elements of solid area, and a horizon-marching method is implemented for it to accelerate the ray-tracing process.

3.2. Surfaces

The surface is triangulated for fast ray-triangle intersection tests into a uniform triangular grid which allows for grid tracing [31] method to be used with run-based ray-traversal [32,33,34] for optimal speed. Horizon mapping is used extensively in the simulation, and several optimized methods to calculate the horizon height to a certain direction are implemented for different situations.

Whether a point $P(x, y)$ on a surface is shadowed from unidirectional radiation $L(\theta_i, \phi_i)$ can be tested in several ways. The basic ray-tracing method is simply to test if a ray from P can escape the surface to the direction of L without intersecting any other surface element. Nevertheless, ray tracing the intersection test for all (θ_i, ϕ_i) is computationally heavy and, in the end, not necessary. More efficient method is to calculate for P the height of the horizon to the direction ϕ_i , i.e., the highest unshadowed value θ_i . When the height of the horizon $\theta_H(\phi)$ is known, we are able to tell if the point is in shadow for arbitrary θ_i .

Two methods for the calculation of $\theta_H(\phi)$ were implemented. For Gaussian surfaces with continuous curvature, the horizon height in $\phi_i = 0$ direction can be calculated from the height-data of the surface vertices along the x -axis, and no ray-tracing methods need to be used. The height of the horizon for a point inside a surface element can be interpolated from the θ_H calculated for the vertices of the surface element. For discontinuous fBm-surfaces this method is not reliable, and ray-tracing is used to search for accurate θ_H .

3.3. The Integrating Hemisphere

Hemisphere Representation

The integrating hemisphere stores the scattering data during the simulation into a quadtree-based data-structure [35]. The tessellation of the hemisphere is carried out with methods based on triangular hierarchical data structures as discussed by Goodchild [36], Dutton [37], Sahr [38], and Kunszt [39]. The upper hemisphere of an octahedron was chosen to form the root of the quadtree, and the subnodes are obtained by subdivision of the geometry (see Fig. 2) using Class I subdivision scheme [38]. The main difference between the current implementation and the cited previous implementations is the use of a half-edge structure to represent the geometry with [17]. This adds some extra memory overhead to the system, but makes the recursive subdivision of the underlying geometry fast, and simplifies the task of finding neighbors for different parts of the structure.

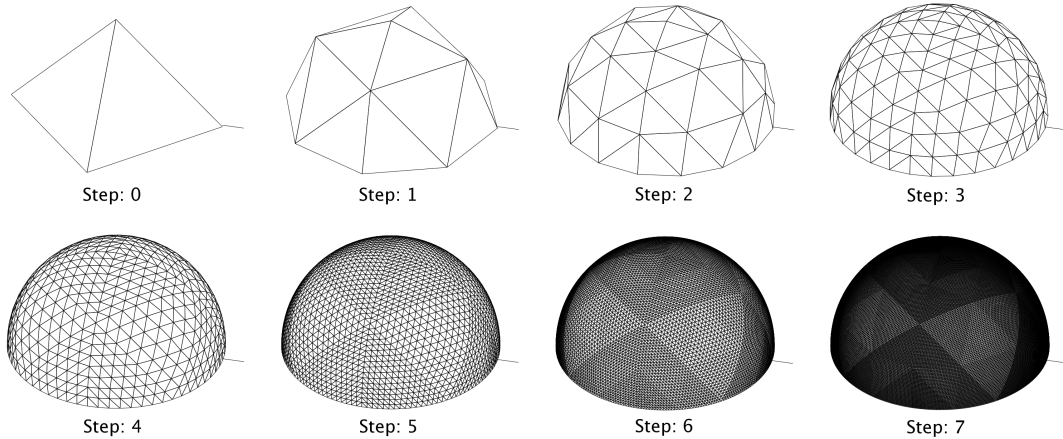


Figure 2. The integrating hemisphere shown with increasing number of subdivisions. During each subdivision, all of the facets (nodes) of the hemisphere are subdivided into four subfacets, and the positions of the new vertices are normalized. This leads to an uneven distribution of solid angles, but is nevertheless better than sampling along constant angles of θ_e and ϕ_e

Two different hemisphere sampling strategies are used. For relatively smooth surfaces, a horizon marching method [17] is utilized to accelerate the search of the elements of the hemisphere, where the radiation may scatter directly from the current surface sample point. For extremely rough surfaces, where the horizon marching method is not applicable, each of the hemisphere elements is sampled separately.

Horizon Marching

Since the surface height is represented by a single-valued single-connected function of two dimensions (x, y) , the height of the horizon θ_h for a point on the surface is a single-valued continuous function of the direction ϕ , $H(\phi) \simeq \theta_h$. The hemisphere from a point on the surface can be factorized into two parts, divided by the horizontal height function. The first part consisting of the directions culled by the surface, and the other of the directions where the radiation can escape directly. If $H = H(\phi)$ can be calculated for a surface sample point, we can immediately evaluate the scattering function to the upper hemisphere, without the need to test each single element for occlusion. For a random rough surface, $H(\phi)$ for an arbitrary point on the surface cannot be calculated analytically, and approximate methods have to be used.

The approximation for a single irradiated surface sample point is started by searching the height of the horizon at $\phi = 0$ in the space of the tessellated hemisphere geometry. After the value for $H(\phi = 0)$ is found, a marching phase starts. The octahedral geometry combined with the half-edge data structure allows one to travel in the hemisphere geometry in an efficient manner. A vertex in the hemisphere geometry is in general connected to six other vertices, the pole, corners, and edges of the octahedron working as special cases. Three of these are in the direction of positive ϕ , and three of negative ϕ . From the first horizon vertex $v_{h, \phi=0}$, we find the lowest unoccluded neighbor vertex in the direction of positive ϕ by testing the three possible traveling directions. The process is repeated from the newfound horizon vertex, and the approximation to $H(\phi)$ is found after marching around the hemisphere. Finally, a scanline-type method is used to select the solid area elements over the horizon.

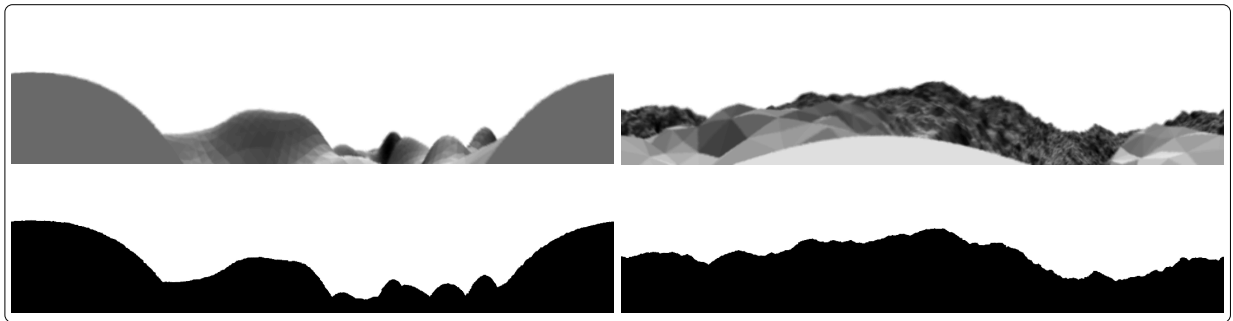


Figure 3. Projections of a rough surface from a single surface sample point to the integrating hemisphere. On the left we show a surface following Gaussian correlation and, on the right, a surface with fBm statistics. The upper subplots show a projection using a full sampling method, and a Lommel-Seeliger scattering law applied to the surface elements. The lower subplots show the horizon of the same points traced using the horizon marching method.

While more complex to implement than the Monte-Carlo or full sampling of the hemisphere, the computation speed is superior to both. The resulting accuracy is comparable to the full sampling, but the number of trace calls needed is around $\frac{1}{20}$ of the full sampling method. The current implementation of the horizon marching method is 12 times faster than the full sampling method implemented. Only when the vertical variation of the horizon line becomes extreme compared to the hemisphere tessellation resolution, i.e. for very rough surfaces, the horizon marching method fails. This can be corrected by adding more possible directions for the method to choose from, thus allowing more complex shapes to be traced, or by changing to the full sampling method.

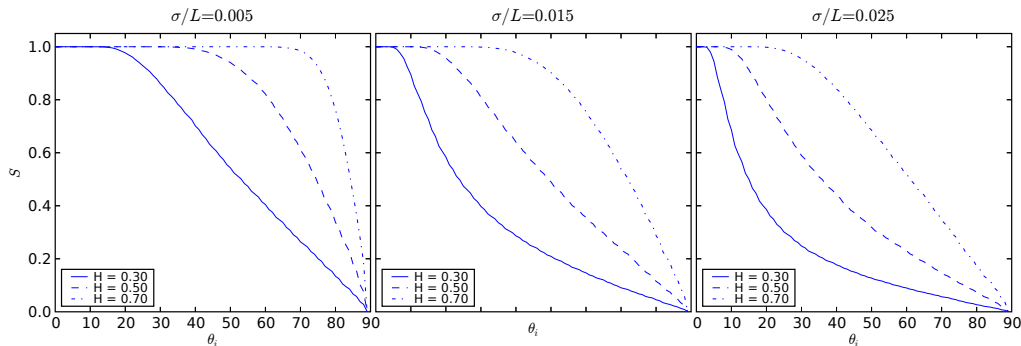


Figure 4. Nadir-viewed shadowing for fBm surfaces as a function of the angle of incidence θ_i .

4. Results and Discussion

We ran the simulations for three distinct BRDF cases. First, we consider geometric shadowing and masking effects independent of any scattering model, next we study the first-order rough-surface scattering effects arising for surfaces with Lambertian scattering elements and, finally, a more realistic case with surfaces consisting of Lommel-Seeliger scattering elements. The Lommel-Seeliger scattering model is of interest on a physical basis, while the Lambertian scattering model is good for comparison with the study by Shkuratov et al. [9]. Two different surface-roughness statistics were used: the Gaussian correlation model and the fBm model. Both models were sampled in the parameter space, and the results for three different H and l are presented, each with three values for $\frac{\sigma}{L}$. The advantage of two fundamentally different surface roughness models is clear: Gaussian surfaces allow us to study the effects arising from a single well-defined scale of roughness features, while fBm surfaces show the effects for surfaces with roughness of all scales, down to the tessellation size of the surface.

The surfaces were generated as 1024×1024 point regular grids with period L of 100.0 units. This leads to the minimum facet edge scale of 0.98 units. The values used for σ were 0.5, 1.5, 2.5, leading to $\frac{\sigma}{L} = 0.005, 0.015, 0.025$, where $\frac{\sigma}{L} = 0.025$ corresponds to an extremely rough surface. For Gaussian surfaces, the correlation lengths l chosen for the study are 1.0, 5.0, 10.0, while for fBm-surfaces we used Hurst-exponents H of 0.3, 0.5, 0.7. The simulations were ran with 200 surface realizations for each set of parameters ($[H, l], \sigma$), and 100 sample points for each realization. Extremely rough surfaces ($H = 0.3$ or $\frac{\sigma}{L} = 0.025$) were simulated using 400 surface realizations and 1600×1600 point surface resolution to ensure good statistics over the whole integrating hemisphere.

The integrating hemisphere was set to subdivision level 6 (see Fig. 2), which results to a mean solid angle per hemisphere facet of 1.4 square arcsecond. Along the constant lines $\phi_e = \frac{n\pi}{2}$, we get $\frac{\pi}{128} \approx 0.025$ radians for the θ_e resolution. Since the major interest of the study is the azimuthal shadowing effect near the back-scattering direction, the results shown are restricted to $\theta_e = [0, \frac{\pi}{2}]$ and $\phi_e = [0, \frac{\pi}{2}]$.

The simulation accuracy was tested by comparing the simulation results against the results obtained from 2048×2048 point surfaces using subdivision level 7 for the integrating hemisphere. The accuracy did not increase significantly for the test cases used.

4.1. Shadowing and Masking

First, we consider pure shadowing and masking effects arising from the surface roughness. The shadowing function $S(\theta_i, \theta_e, \Delta\phi)$ gives us the probability that a surface point is both visible and not shadowed. Geometrically this is equivalent to the ratio of the irradiated surface area projected to a plane with normal (θ_e, ϕ_e) , to the total surface area projected to the same plane.

The nadir-viewed geometric shadowing shown in Figs. 4 and 5 can be compared to the study made by Shepard and Campbell [10]. The main result visible from the figures is well known: the steepness of the shadowing function depends strongly on the scale of the surface roughness features. Small-scale roughness

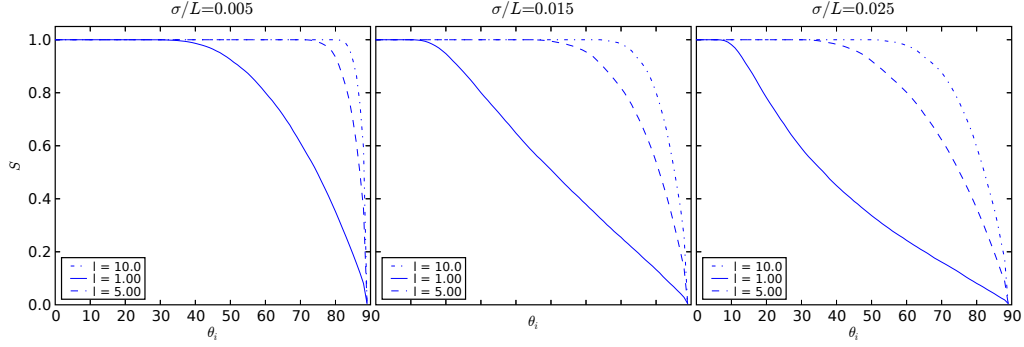


Figure 5. As in Fig. 4 for surfaces with Gaussian correlation.

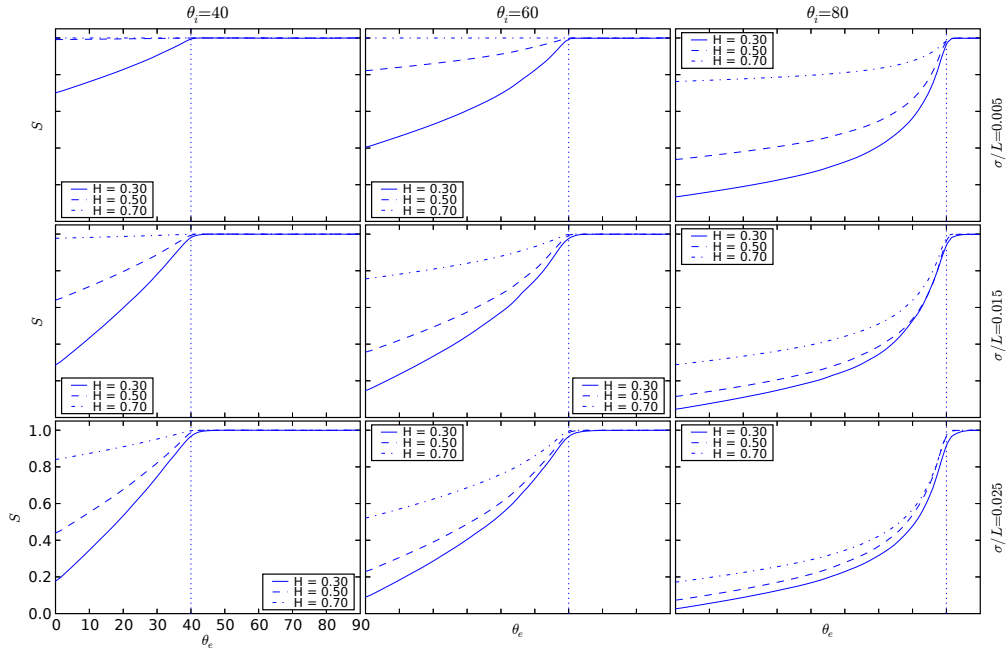


Figure 6. Combined shadowing and masking function along $\phi_e = 0$ for fBm surfaces as a function of the angle of emergent radiation θ_e . Shown are plots for three different angles of incident radiation θ_i , three different $\frac{\sigma}{L}$, and three different H . The backscattering angle is drawn for each plot as a dotted vertical line.

has a greater contribution to the shadowing than the large-scale roughness of equivalent amplitude. Figures 6 and 7 show the shadowing function along constant azimuth angle $\phi_e = 0$, as a function of the angle of emergent radiation θ_e . As θ_e approaches the backscattering direction θ_i , the shadowing function approaches unity. For $\theta_e > \theta_i$, no shadows are visible. Small-scale roughness ($H = 0.3$ or $\frac{l}{L} = 0.01$) can be seen to have a notable effect for even modest roughness amplitudes. For the most extreme cases where $\frac{\sigma}{L} = 0.025$, shadowing in all the simulated fBm surfaces approaches a similar form together with increasing θ_i . Figures 8 and 9 show the shape of the azimuthal shadowing effect along constant $\theta_e = \theta_i$ as a function of the azimuth angle ϕ_e . For most situations, the shadowing function can be considered linear for $20^\circ < \Delta\phi < 90^\circ$.

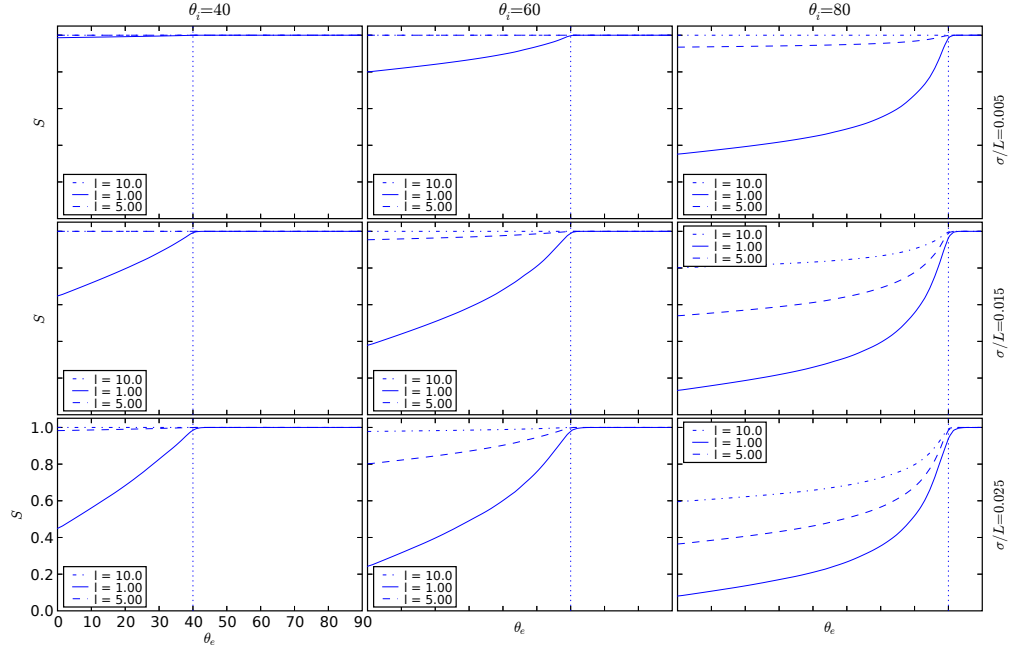


Figure 7. As in Fig. 6 for surfaces with Gaussian correlation.

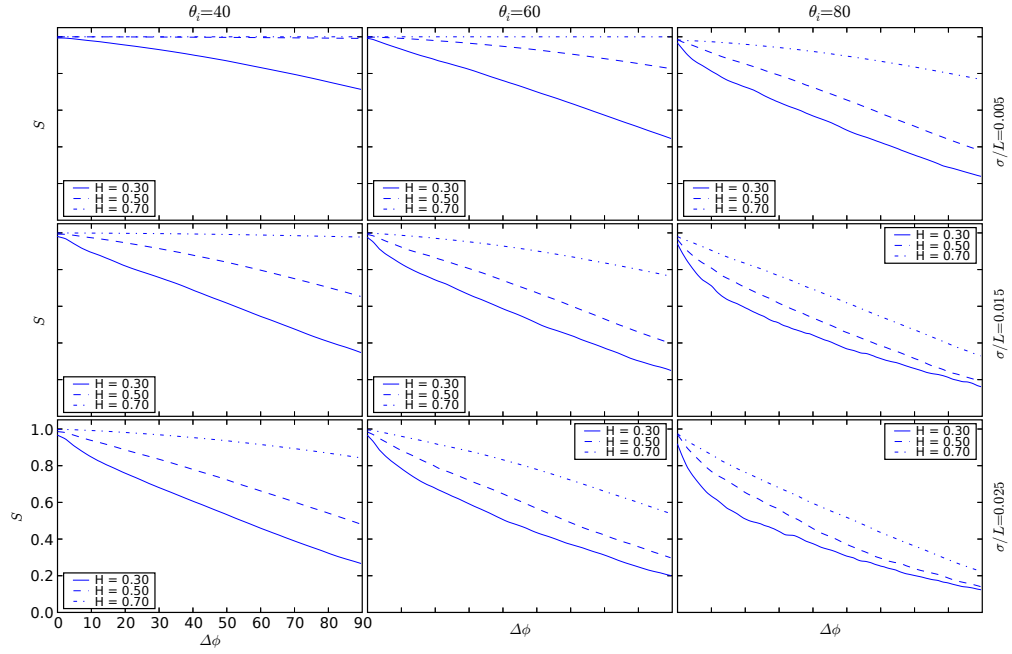


Figure 8. Shadowing for fBm-surfaces as a function of azimuth angle ϕ_e and constant $\theta_e = \theta_i$. The shape of the azimuthal shadowing effect is seen as a function of varying surface geometry.

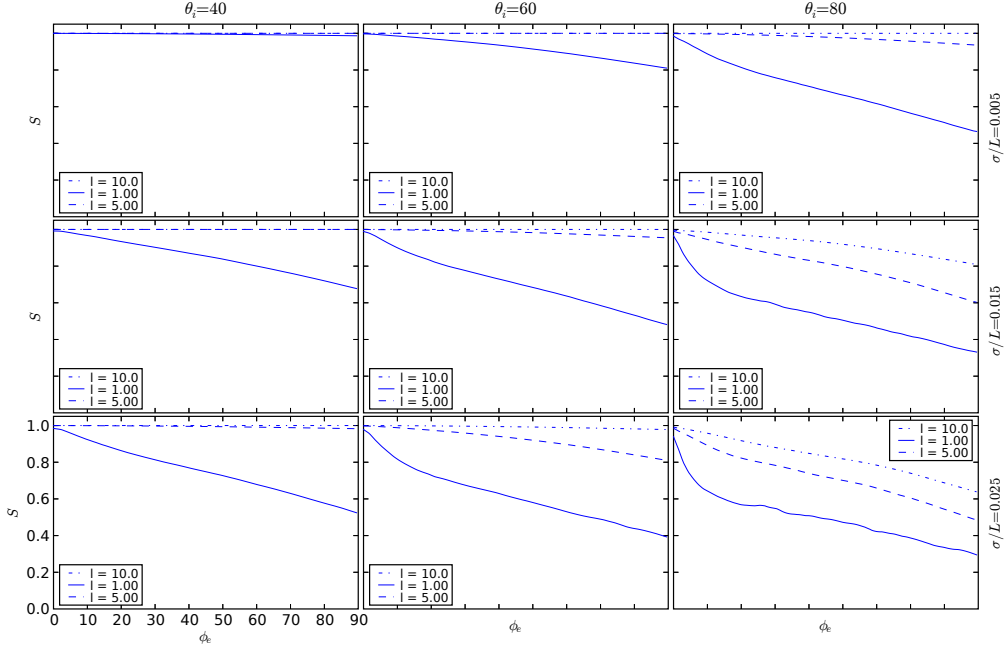


Figure 9. As in Fig. 8 for surfaces with Gaussian correlation.

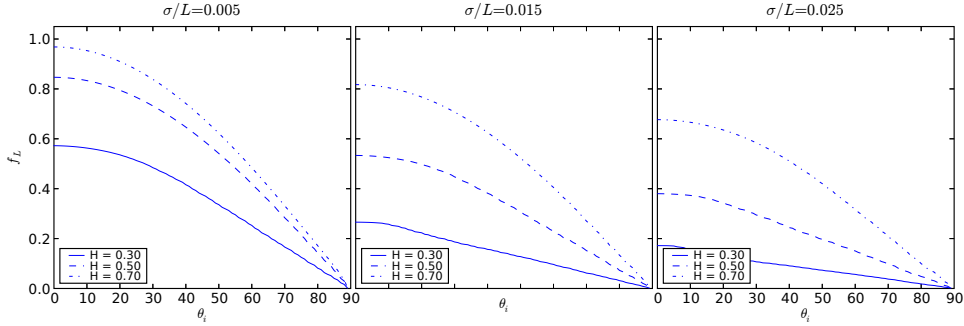


Figure 10. As in Fig. 4 for a surface with Lambertian scattering elements.

4.2. Lambertian Surfaces

Next, the behaviour of rough surfaces with Lambertian scattering elements was considered. The simulations were carried out using the same sets of parameters as for the pure shadowing-function studies. Now, the observed radiance is a function of the distribution of the normals of the visible unshadowed surface elements, as well as of the ratio of visible unshadowed surface elements to the total visible surface area.

The nadir-viewed rough-surface-corrected Lambertian BRDF $f_{L,RS}$ multiplied by 4π is shown in Figs. 10 and 11. The z -component of the normals of the surface elements decreases with increasing surface roughness amplitude, i.e., the rms-slope of the surface increases, and the radiance observed from the nadir decreases for all θ_i . For surfaces with Gaussian correlation function, only the smallest-scale roughness ($\frac{l}{L} = 0.01$) has a significant effect on the shape of the curve. For fBm surfaces, the smaller values of H yield more notable effects, as can be expected. The similarity between the nadir-viewed values of fBm surfaces with $H = 0.5$ and Gaussian correlation surfaces with $\frac{l}{L} = 0.01$ is interesting. Figures 12 and 13 show $f_{L,RS}$ in a similar fashion to Figs. 6 and 7. For a smooth surface, the value of f_L is constant for constant θ_i . This is also the

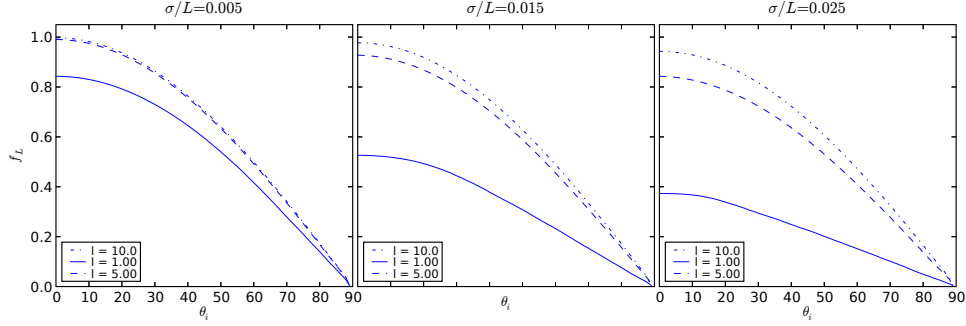


Figure 11. As in Fig. 5 for a surface with Lambertian scattering elements.

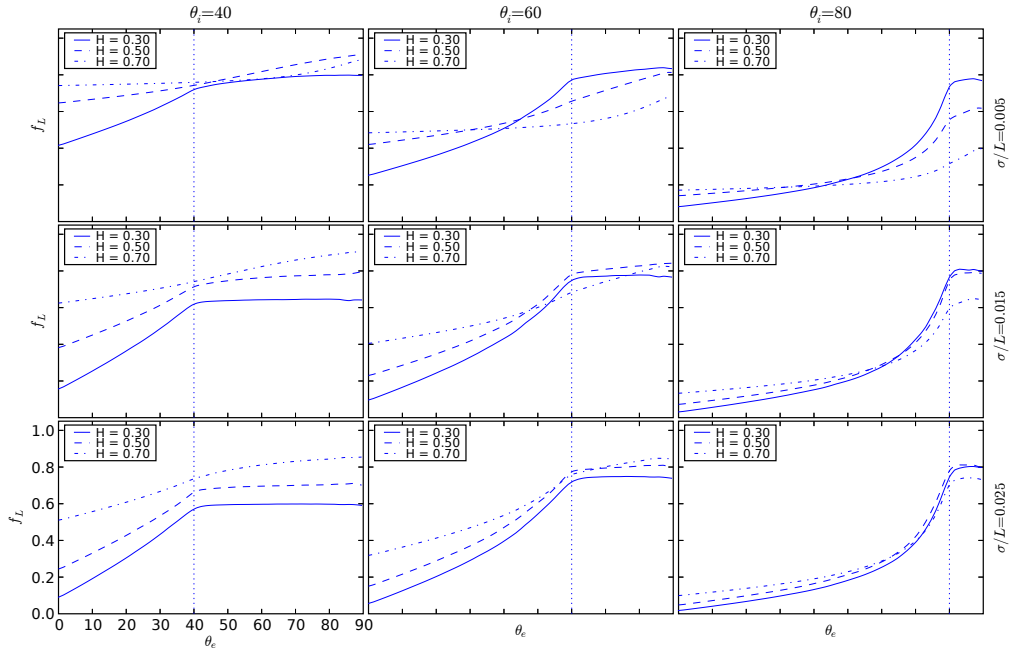


Figure 12. As in Fig. 6 for a surface with Lambertian scattering elements.

case for surfaces with only large-scale roughness features of small amplitude. Small-scale roughness creates rather a sharp change in the slope of the curve in the backscattering direction $\theta_e = \theta_i$. Figures 14 and 15 show the behaviour of the $f_{L,RS}$ as a function of the azimuth-angle. The azimuthal behaviour is still similar for the fBm surfaces with $H = 0.5$ and Gaussian correlation surfaces with $\frac{l}{L} = 0.01$, but breaks down when moving to large θ_i and extreme roughness amplitudes.

4.3. Lommel-Seeliger Surfaces

Finally, the behaviour of rough surfaces with Lommel-Seeliger scattering elements was studied. As for the Lambertian BRDF, the simulations were carried out using the same sets of parameters as for the pure shadowing function studies.

The nadir-viewed rough-surface corrected Lommel-Seeliger BRDF $4\pi f_{LS,RS}$ is shown in Figs. 16 and 17. The behaviour differs both from the pure shadowing function and the rough-surface-corrected Lambertian BRDF. The most notable feature is that for the backscattering geometry $\theta_e = \theta_i$, $4\pi f_{LS,RS} = \frac{1}{2}$, something

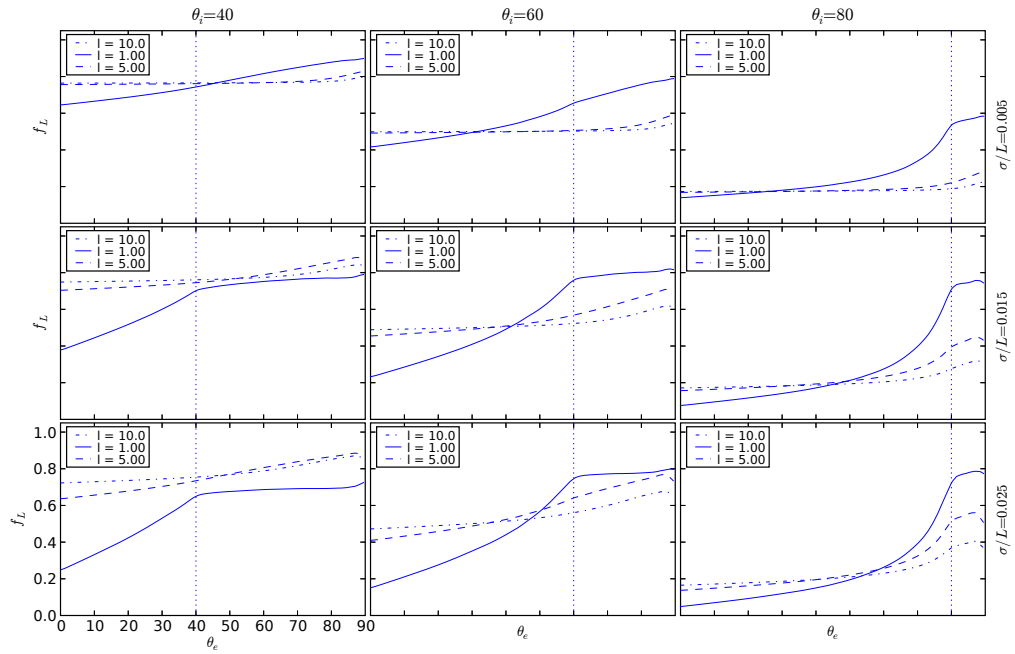


Figure 13. As in Fig. 7 for a surface with Lambertian scattering elements..

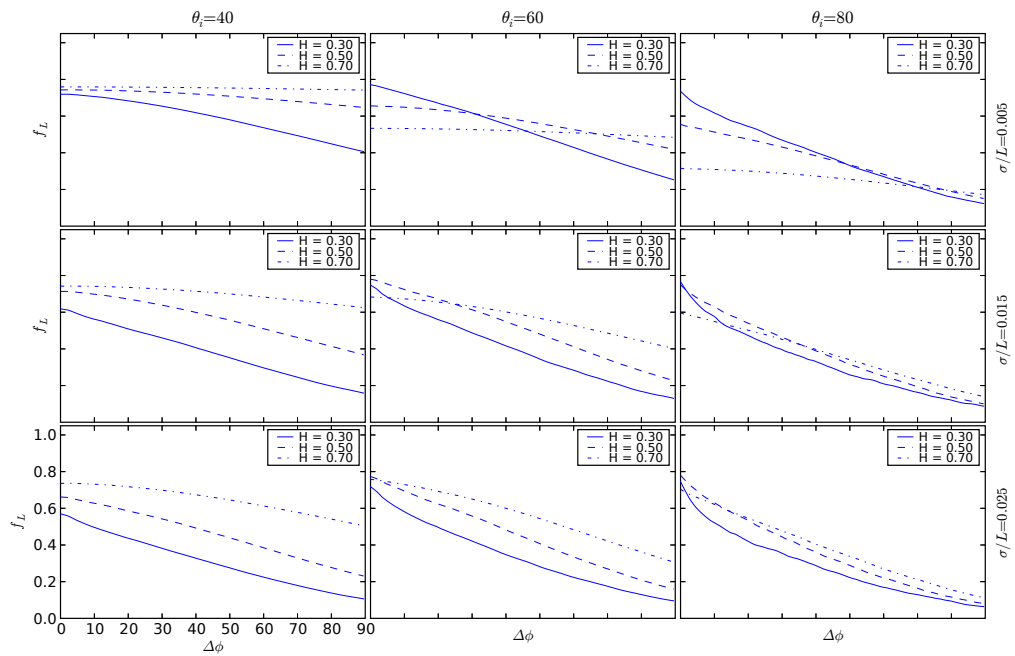


Figure 14. As in Fig. 8 for a surface with Lambertian scattering elements.

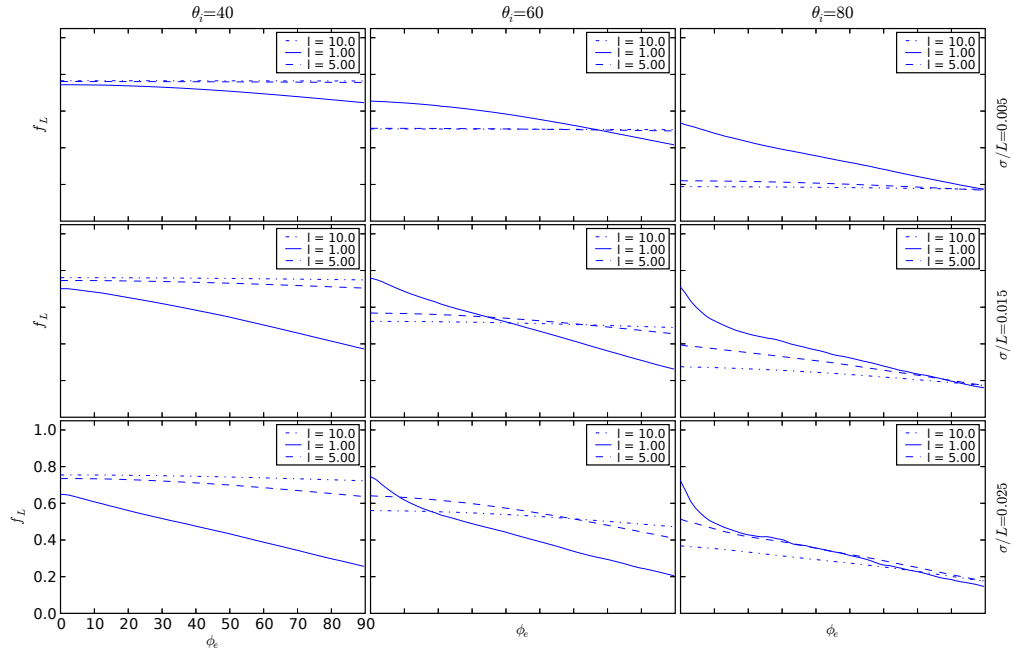


Figure 15. As in Fig. 9 for a surface with Lambertian scattering elements.

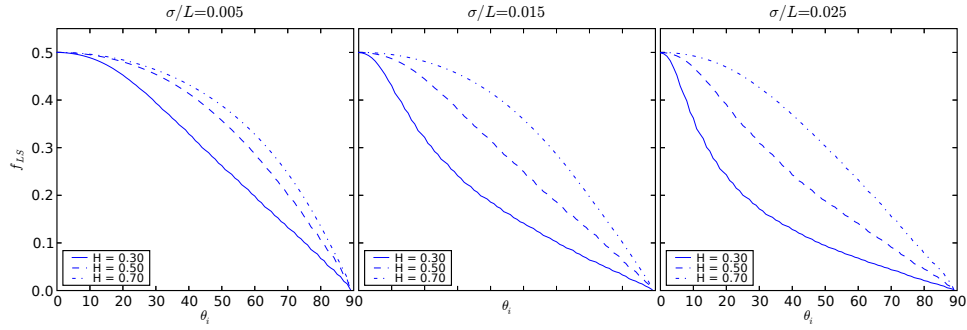


Figure 16. As in Fig. 4 for a surface with Lommel-Seeliger scattering elements.

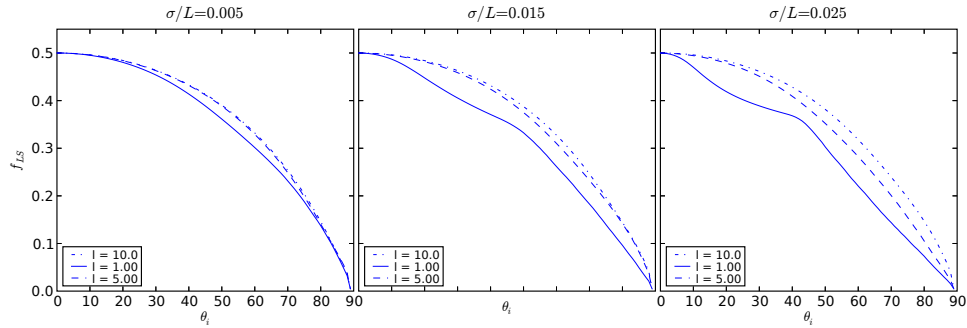


Figure 17. As in Fig. 5 for a surface with Lommel-Seeliger scattering elements.

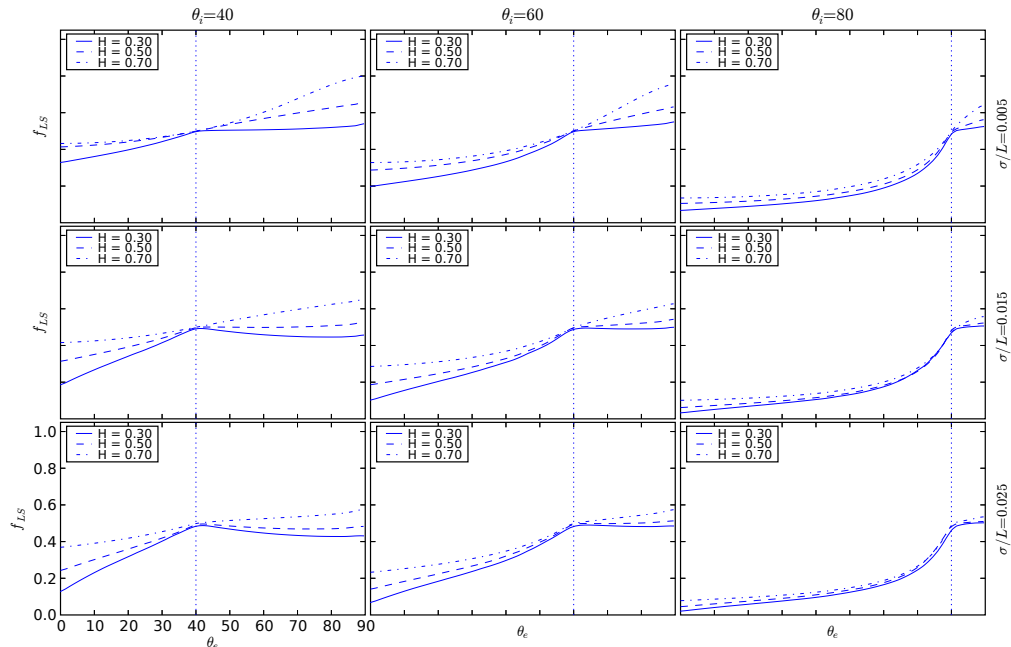


Figure 18. As in Fig. 6 for a surface with Lommel-Seeliger scattering elements.

that can be also be seen from Figs. 18, 19, 20, and 21. This is due to the $\frac{\mu_0}{\mu + \mu_0}$ dependence of the Lommel-Seeliger scattering law. For the backscattering geometry with $\mu = \mu_0$, which results in $f_{LS,RS} = \frac{1}{4\pi}$, unlike for the Lambertian scattering model, the distribution of surface slopes does not matter.

Figure 22 shows the basic Lommel-Seeliger BRDF $4\pi f_{LS}$ mapped to spherical coordinates ($\theta = \Delta\phi, r = \theta_e$), $\Delta\phi = [0 \dots 2\pi]$, $\theta = [0 \dots \frac{\pi}{2}]$. The brightness value is linearly mapped to $[0 \dots 1]$, black = 0, white = 1. Figures 23 and 24 show the behaviour of $f_{LS,RS}$ for fBm surfaces with $H = 0.3, 0.5, 0.7$, $\frac{\sigma}{L} = 0.005, 0.025$, and $\theta_i = 0^\circ, 20^\circ, 40^\circ, 60^\circ, 80^\circ$. The geometric rough-surface shadowing effect is clearly visible for surfaces with $H = 0.3$, and can be distinguished as well from the surface $H = 0.5$, $\frac{\sigma}{L} = 0.015$.

4.4. Discussion

Rough-surface shadowing has been studied, together with rough-surface-corrected Lambert and Lommel-Seeliger reflectance functions. Since the paper discusses only the first-order scattering effects in the geometric-optics regime, it applies to bodies with low single-scattering albedo $\tilde{\omega}$. The importance of multiple scattering increases together with increasing $\tilde{\omega}$ and, for simulations of bright objects, computation of several orders of scattering is necessary. Multiple scattering between surface roughness elements is considered to fade the geometric shadowing effects and smoothen the reflectance model [9]. Inclusion of multiple scattering to the simulation would make $\tilde{\omega}$ an extra parameter to the resulting scattering model, though different levels of scattering could be possible to separate from each other. Another important factor, when the surface-roughness features are small considered to the mean free path of the radiation inside the scattering medium, is the subsurface scattering. Subsurface scattering would also smoothen the effects from shadowing and masking, but would include the absolute scale dependency, as well as the dependency on the scattering parameters of the medium.

Shadowing arising from fBm surfaces depends on the Hurst-exponent H . Decreasing H leads to increasing power for small-scale roughness features. The smaller-scale roughness features have a stronger effect on the shadowing of the surface. Thus, a rough surface with small H and relatively small surface-roughness amplitude shows much greater shadowing than a surface with larger H and roughness amplitude. For surfaces

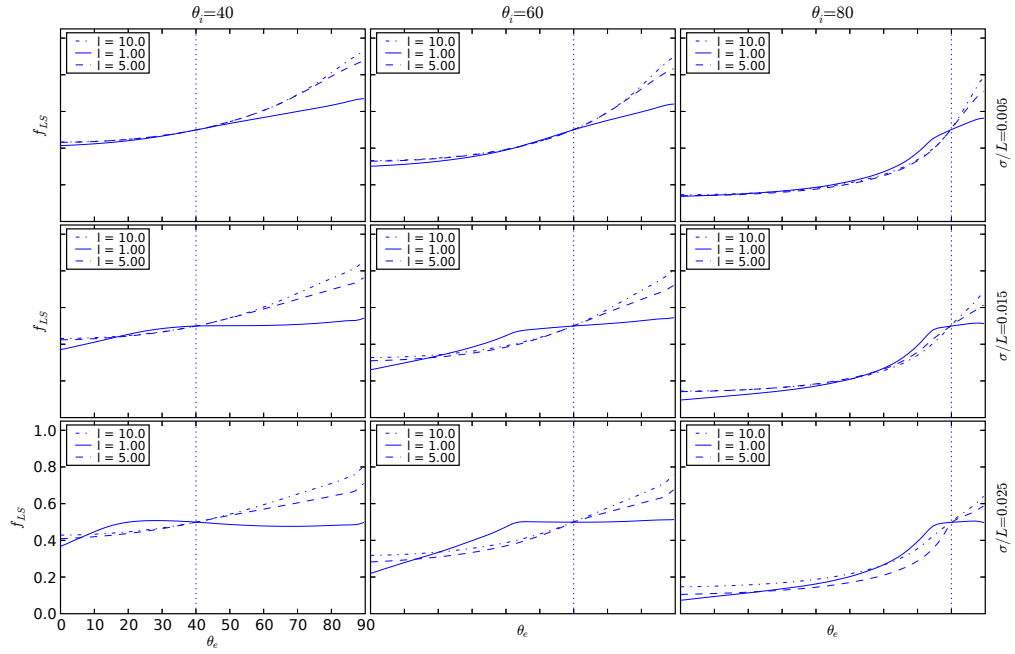


Figure 19. As in Fig. 7 for a surface with Lommel-Seeliger scattering elements.

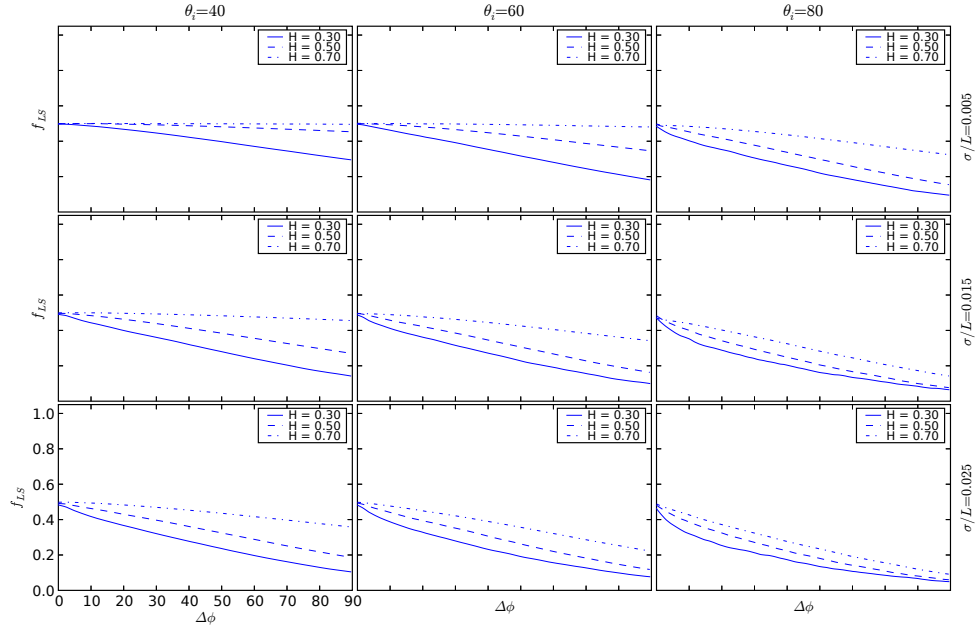


Figure 20. As in Fig. 8 for a surface with Lommel-Seeliger scattering elements.

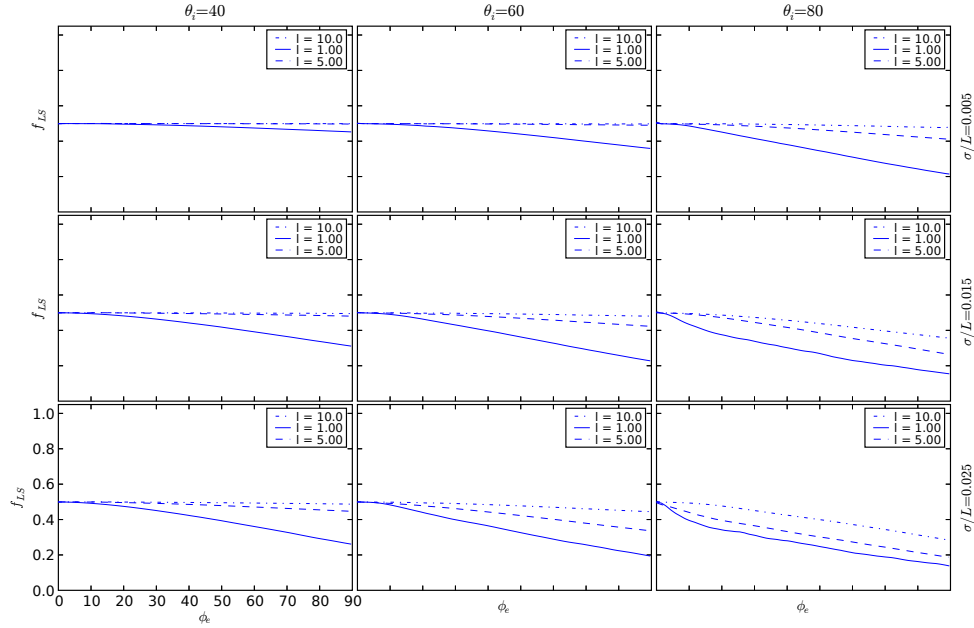


Figure 21. As in Fig. 9 for a surface with Lommel-Seeliger scattering elements.

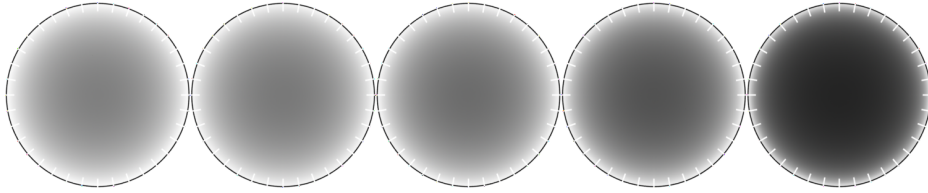


Figure 22. Lommel-Seeliger BRDF for $\theta_i = 0^\circ, 20^\circ, 40^\circ, 60^\circ, 80^\circ$.

with only one major roughness scale, the angular dependence of shadowing, when moving away from the opposition geometry, depends strongly on the ratio $\frac{\sigma}{l}$. The behavior of shadowing from the opposition direction as a function of the azimuth angle is almost linear in the range $\Delta\phi = [0 \dots \frac{\pi}{2}]$ for fBm surfaces with large H . For smaller H , a nonlinear brightening can be observed. The same results apply to surfaces with Lommel-Seeliger scattering elements.

Acknowledgements

We thank the anonymous referee for helpful and constructive comments. Research was supported, in part, by the Academy of Finland.

References

- [1] K. Lumme, E. Bowell, Radiative transfer in the surfaces of atmosphereless bodies. I - Theory. II - Interpretation of phase curves, AJ 86 (1981) 1694–1721.
- [2] K. Lumme, W. M. Irvine, Radiative transfer in the surfaces of atmosphereless bodies. III - Interpretation of lunar photometry, AJ 87 (1982) 1076–1082.
- [3] B. Hapke, Bidirectional reflectance spectroscopy. I - Theory, J. Geophys. Res. 86 (1981) 3039–3054.

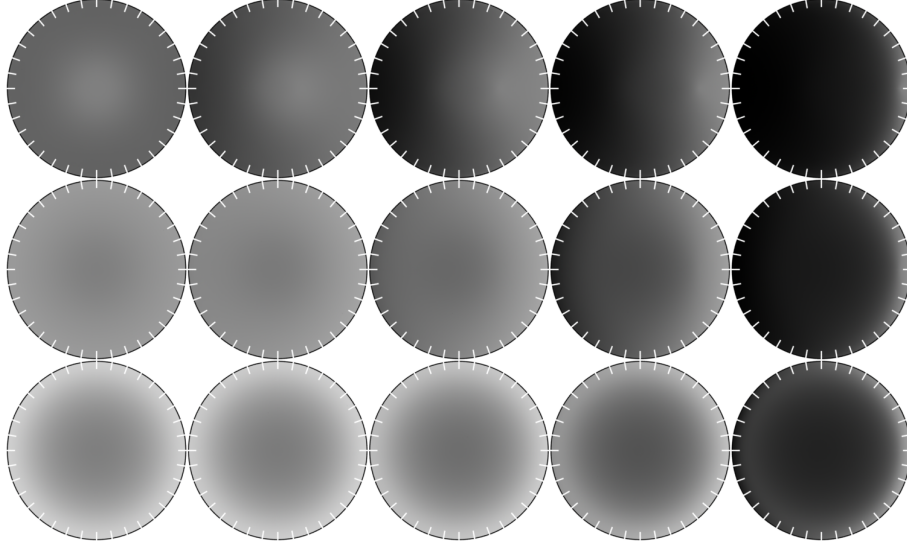


Figure 23. $f_{LS,RS}$ with $\frac{\sigma}{L} = 0.005$, $H = 0.3, 0.5, 0.7$, $\theta_i = 0^\circ, 20^\circ, 40^\circ, 60^\circ, 80^\circ$.

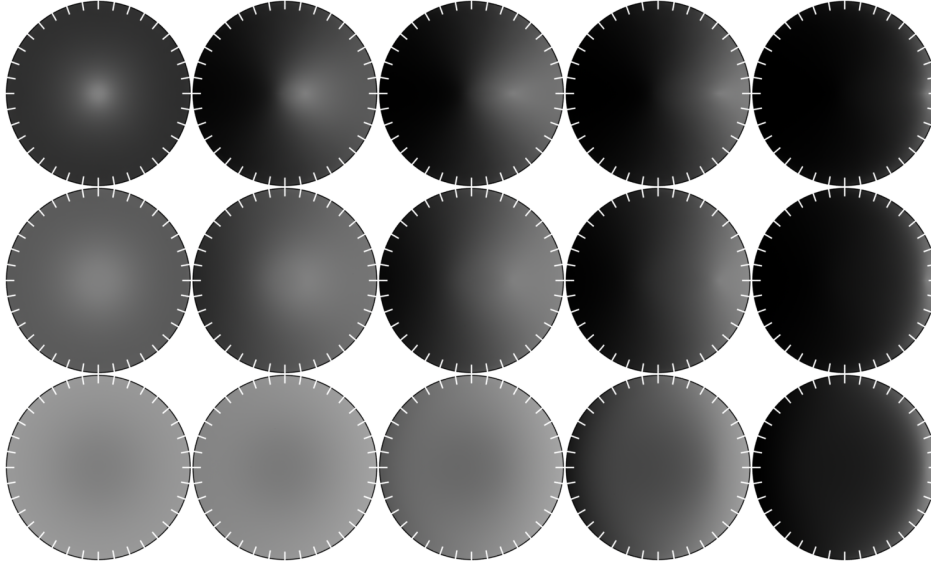


Figure 24. $f_{LS,RS}$ with $\frac{\sigma}{L} = 0.015$, $H = 0.3, 0.5, 0.7$, $\theta_i = 0^\circ, 20^\circ, 40^\circ, 60^\circ, 80^\circ$.

- [4] B. Hapke, Bidirectional reflectance spectroscopy. III - Correction for macroscopic roughness, *Icarus* 59 (1984) 41–59. doi:10.1016/0019-1035(84)90054-X.
- [5] K. Lumme, J. Peltoniemi, W. M. Irvine, Diffuse reflection from a stochastically bounded, semi-infinite medium, *Transport Theory and Statistical Physics* (1990) 317–332.
- [6] K. Lumme, J. I. Peltoniemi, W. M. Irvine, Derivation of an Average Single Particle Phase Function for the Lunar Regolith, in: *Lunar and Planetary Institute Conference Abstracts*, 1989, pp. 606–+.
- [7] J. Peltoniemi, Light scattering in planetary regoliths and cloudy atmospheres, Ph.D. thesis, University of Helsinki (1993).
- [8] Y. Shkuratov, A. Ovcharenko, E. Zubko, O. Miloslavskaya, K. Muinonen, J. Piironen, R. Nelson, W. Smythe, V. Rosenbush, P. Helfenstein, The Opposition Effect and Negative Polarization of Structural Analogs for Planetary Regoliths, *Icarus* 159 (2002) 396–416. doi:10.1006/icar.2002.6923.
- [9] Y. G. Shkuratov, D. G. Stankevich, D. V. Petrov, P. C. Pinet, A. M. Cord, Y. H. Daydou, S. D. Chevrel, Interpreting photometry of regolith-like surfaces with different topographies: shadowing and multiple scattering, *Icarus* 173 (2005) 3–15.

doi:10.1016/j.icarus.2003.12.017.

- [10] M. K. Shepard, B. A. Campbell, Shadows on a Planetary Surface and Implications for Photometric Roughness, *Icarus* 134 (1998) 279–291. doi:10.1006/icar.1998.5958.
- [11] M. K. Shepard, B. A. Campbell, Radar Scattering from a Self-Affine Fractal Surface: Near-Nadir Regime, *Icarus* 141 (1999) 156–171. doi:10.1006/icar.1999.6141.
- [12] M. K. Shepard, B. A. Campbell, M. H. Bulmer, T. G. Farr, L. R. Gaddis, J. J. Plaut, The roughness of natural terrain: A planetary and remote sensing perspective, *Journal of Geophysical Research* 106 (2001) 32777–32796. doi:10.1029/2000JE001429.
- [13] K. Muinonen, K. Lumme, J. I. Peltoniemi, W. M. Irvine, Statistical Photoclinometry and Surface Topography of Atmosphereless Bodies, in: C. I. Lagerkvist, H. Rickman, B. A. Lindblad (Eds.), *Asteroids, Comets, Meteors III*, 1990, pp. 155–+.
- [14] A. Penttilä, Numerical solution to the first-order light scattering by rough and particulate surfaces, in: *Proceedings of the 8th Conference on Electromagnetic and Light Scattering by Nonspherical Particles: Theory, Measurements and Applications*, 2005, pp. 265–268.
- [15] F. E. Nicodemus, J. C. Richmond, J. J. Hsia, I. W. Ginsberg, T. Limperis, Geometric Considerations and Nomenclature for Reflectance, Monograph 161, National Bureau of Standards (US) (Oct. 1977).
- [16] T. P. Lester, M. L. McCall, J. B. Tatum, Theory of planetary photometry, *The Journal of the Royal Astronomical Society of Canada* 73 (1979) 233–257.
- [17] H. Parviainen, Ray tracing model for light scattering from self-affine random rough surfaces, Master’s thesis, University of Helsinki (2006).
- [18] F. X. Sillion, J. R. Arvo, S. H. Westin, D. P. Greenberg, A global illumination solution for general reflectance distributions, in: *SIGGRAPH ’91: Proceedings of the 18th annual conference on Computer graphics and interactive techniques*, ACM Press, New York, NY, USA, 1991, pp. 187–196. doi:http://doi.acm.org/10.1145/122718.122739.
- [19] S. H. Westin, J. R. Arvo, K. E. Torrance, Predicting reflectance functions from complex surfaces, in: *SIGGRAPH ’92: Proceedings of the 19th annual conference on Computer graphics and interactive techniques*, ACM Press, New York, NY, USA, 1992, pp. 255–264. doi:http://doi.acm.org/10.1145/133994.134075.
- [20] S. H. Westin, Predicting reflectance functions from complex surfaces, Master’s thesis, Cornell University (1992).
- [21] P. Gautron, J. Krřivánek, S. N. Pattanaik, K. Bouatouch, A novel hemispherical basis for accurate and efficient rendering, in: *Rendering Techniques 2004, Eurographics Symposium on Rendering*, 2004, pp. 321–330. URL citeseer.ist.psu.edu/gautron04novel.html
- [22] J. J. Koenderink, A. J. van Doorn, A. Stavridi, Bidirectional reflection distribution function expressed in terms of surface scattering modes, in: *ECCV ’96: Proceedings of the 4th European Conference on Computer Vision-Volume II*, Springer-Verlag, London, UK, 1996, pp. 28–39.
- [23] P. Schröder, W. Sweldens, Spherical wavelets: Efficiently representing functions on the sphere, in: *SIGGRAPH ’95: Proceedings of the 22nd annual conference on Computer graphics and interactive techniques*, ACM Press, New York, NY, USA, 1995, pp. 161–172. doi:http://doi.acm.org/10.1145/218380.218439.
- [24] R. J. Adler, *The Geometry of Random Fields*, Wiley, 1981.
- [25] C. Preston, *Random Fields*, Springer-Verlag, 1976.
- [26] I. A. Ibragimov, Y. A. Rozanov, *Gaussian Random Processes*, Springer-Verlag, 1970.
- [27] G. A. Fenton, Simulation and analysis of random fields, Ph.D. thesis, Princeton University (1990).
- [28] H. O. Peitgen, S. Saupe (Eds.), *The Science of Fractal Images*, Springer-Verlag, 1988.
- [29] T. Dieker, Simulation of fractional brownian motion, Master’s thesis, University of Twente (2002).
- [30] M. Pharr, G. Humphreys, *Physically Based Rendering*, Morgan Kaufmann, 2004.
- [31] F. K. Musgrave, C. E. Kolb, R. S. Mace, The synthesis and rendering of eroded fractal terrains, in: *SIGGRAPH ’89: Proceedings of the 16th annual conference on Computer graphics and interactive techniques*, ACM Press, New York, NY, USA, 1989, pp. 41–50. doi:http://doi.acm.org/10.1145/74333.74337.
- [32] P. Stephenson, The structure of digitised line: With applications to line drawing and ray tracing in computer graphics, Ph.D. thesis, James Cook University of North Queensland (1998).
- [33] P. Stephenson, B. Litow, Why step when you can run? iterative line digitization algorithms based on hierarchies of runs, *IEEE Comput. Graph. Appl.* 20 (6) (2000) 76–84. doi:http://dx.doi.org/10.1109/38.888021.
- [34] P. Stephenson, B. Litow, Making the dda run: two-dimensional ray traversal using runs and runs of runs, in: *ACSC ’01: Proceedings of the 24th Australasian conference on Computer science*, IEEE Computer Society, Washington, DC, USA, 2001, pp. 177–183.

- [35] P. Barrett, Application of the Linear Quadtree to Astronomical Databases, in: ASP Conf. Ser. 77: Astronomical Data Analysis Software and Systems IV, 1995, pp. 472–+.
- [36] M. F. Goodchild, Spatial data representation and basic operations for a triangular heirarchical data structure, Tech. rep., National Center for Geographic Information Analysis, University of California, Santa Barbara (1991).
- [37] G. Dutton, Encoding and handling geospatial data with hierarchical triangular meshes, in: Advances in GIS Research II, 1996.
- [38] K. Sahr, D. White, A. Jon Kimerling, Geodesic discrete global grid systems, *Cartography and geographic information science* 30 (2) (2003) 121–134.
- [39] P. Z. Kunszt, A. S. Szalay, A. R. Thakar, The Hierarchical Triangular Mesh, in: *Mining the Sky*, 2001, pp. 631–+.